DOI: https://doi.org/10.1016/j.ymssp.2019.07.011

Novel Discrete Frequency-Phase Modulated Excitation Waveform for Enhanced Depth Resolvability of Thermal Wave Radar

Saeid Hedayatrasa [1,2*], Gaétan Poelman[1,2], Joost Segers[1], Wim Van Paepegem[1] and Mathias Kersemans[1]

[1] Mechanics of Materials and Structures (UGent-MMS), Department of Materials, Textiles and Chemical Engineering, Ghent University, Technologiepark-Zwijnaarde 46, 9052 Zwijnaarde, Belgium

[2]SIM Program M3 DETECT-IV, Technologiepark-Zwijnaarde 48, B-9052 Zwijnaarde, Belgium

[*]saeid.hedayatrasa@ugent.be

Abstract

Thermal wave radar (TWR) is a state-of-the-art non-destructive testing method, inspired by radio wave radar systems, in order to increase depth resolution and signal to noise ratio of optical infrared thermography through pulse compression. Analogue frequency modulation (i.e. frequency sweep) and Barker binary phase modulation are the two popular and widely researched pulse compression techniques in TWR among which Barker coding has shown the highest performance. This paper introduces a novel modulated waveform with variable discrete frequency-phase modulation (FPM) which distinctively enhances the depth resolvability of TWR compared to the existing techniques. The pulse compression quality and depth resolvability of the novel FPM waveform is initially evaluated through a 1D analytical solution. The analogue frequency modulated and discrete phase modulated waveforms as well as mono-frequency excitation (i.e. lock-in thermography) are also evaluated at the same central frequency as the reference. Objective functions are defined and a large search space is explored for optimal modulation codes. Two FPM waveforms are selected based on their maximized depth resolvability through resultant lag and phase in the output channel of TWR. Furthermore, the excellent performance of the selected FPM waveforms is validated by 3D finite element simulation. A delaminated glass fiber reinforced polymer (GFRP) laminate is simulated in order to evaluate the impact of a dominant lateral heat diffusion on the performance of the novel FPM waveforms. The superior depth resolvability of the introduced FPM waveforms is confirmed and their robustness at various noise levels is demonstrated.

Keywords**:** Infrared Thermography; Radar; Waveform; Pulse Compression; Composite

1. Introduction

Optical infrared thermography is an efficient nondestructive testing (NDT) method for full-field remote inspection of a relatively large area of a test piece [1, 2]. An optical source radiates heat onto the inspection surface and a high sensitivity infrared camera records the resultant thermal images. The stimulated heat wave diffuses through the thickness of the sample and interacts with the internal defects due to the thermal diffusivity mismatch introduced by their interfaces. Then, the defects can be detected and quantified through their impact on the evolution of the surface temperature. The technique is mainly limited by the diffusive nature of the heat wave as its amplitude exponentially decays over the space and (contrary to elastic waves) lacks a wavefront to provide high incident energy. Developments of adequate excitation and post-processing

DOI: https://doi.org/10.1016/j.ymssp.2019.07.011

techniques to overcome the current detectability limits of infrared thermography and to obtain proper quantification of defects have been widely researched (e.g. [3-6]).

Thermal wave radar (TWR) is a state-of-the-art technique developed for increased depth resolution and signal to noise ratio (SNR) of infrared thermography, applied in optical thermography using laser or halogen/LED lamps [7-16] and more recently in eddy current induction thermography [17, 18]. TWR is based on pulse compression techniques originally implemented in the radio wave radar (RAdio Detection And Ranging) systems [19, 20]. Cross-correlation of the echo reflected from an object with the transmitted waveform enables a radar system to determine the object's range by searching the peak and corresponding time delay (lag) or phase in the output channel of the matched filter. In practice, the presence of stochastic noise and the possibility of overlapping echoes from multiple closely spaced objects, leads to ambiguity in the detection of the peak corresponding to an object. Although transmission of very short pulses can increase the range resolution, it results in a lower SNR due to the low energy input. The pulse compression technique overcomes this limitation through the transmission of a long but modulated waveform. A properly modulated waveform compresses the energy of the cross-correlated signal under its main lobe and leads to an increased range resolution and a high SNR. The modulated waveforms commonly used in radio wave radar are: analogue linear frequency modulation (sweep), discrete frequency modulation (e.g. Costas coding), discrete phase modulation (e.g. Barker and Franck coding) [20], and frequency and/or phase modulation by optimization [21, 22].

Contrary to the radio wave radar, TWR deals with a dispersive and overly-damped thermal response associated with the diffusive nature of heat waves. Therefore, the measured thermal response at the surface of a specimen is not a reflected replica of the input excitation waveform anymore, but becomes distorted. The surface temperature is primarily affected by the heat capacity of the specimen which acts as a low pass filter. Moreover, it experiences a time varying phase delay depending on (i) the frequency spectrum induced by the excitation waveform and (ii) the depth of the internal scatters (i.e. defect interfaces).

On the other hand, in lock-in thermography (LT) a mono-frequency harmonic excitation is applied to the specimen which resolves the depth proportional to its diffusivity length. Hence, the application of TWR through a modulated waveform around the same frequency increases the bandwidth of the excitation spectrum and enhances the depth resolvability by an increased probing depth and increased depth resolution. However, the time varying phase delay of the thermal response (which follows the modulation introduced by the waveform) may have an accumulating or a dissolving contribution to the output lag or phase channel of the cross-correlation. This can explain why a Barker coded waveform can lead to a higher depth resolvability compared to a relatively wideband sweep around the same frequency [15, 23].

The aforementioned deviation of the thermal response with respect to the excitation waveform complicates the implementation of TWR compared to the radio wave radar. However, the research presented in this paper opens new insights and opportunities for systematic thermal adaptation of the modulated waveform so that a maximized depth resolvability is achieved through TWR.

In this paper, a novel frequency-phase modulated (FPM) waveform is introduced and its discrete modulation code is adapted in order to maximize the depth resolvability of TWR. Initially, the thermal frequency response is calculated through a simplified 1D analytical solution for fast and efficient exploration of supreme FPM waveforms. Then the enhanced depth resolvability of

DOI: https://doi.org/10.1016/j.ymssp.2019.07.011

the obtained FPM waveforms, compared to the conventional waveforms, is validated through 3D finite element (FE) simulation. A glass fiber reinforced polymer (GFRP) laminate with the quasi-isotropic lay-up $[+45/0/-45/90]_{2s}$ and a thickness of 4 mm is simulated to be inspected for the detection of delaminations.

2. Theory of thermal wave radar (TWR)

TWR is implemented by matched filtering of the measured thermal response with the excitation waveform [7-9]. The matched filter is an optimal linear filter which maximizes the SNR in the presence of stochastic noise and reaches its maximum value at a delay time corresponding to the depth of the defect. Matched filtering is typically done by time-domain cross-correlation of the measured thermal response $\tilde{T}(t)$ with the corresponding excitation (reference) waveform $\tilde{S}(t)$ as follows [20]:

$$\chi(\tau) = \tilde{T}(t) \otimes \tilde{S}(t+\tau) = \int_{-\infty}^{+\infty} \tilde{T}(t)\tilde{S}(t+\tau)dt \quad (1)$$

where $\otimes$ denotes cross-correlation and ($\tilde{}$) denotes the AC component of the signal due to the mono-polar nature of optical excitation. For computational efficiency the cross-correlation is preferably performed in the frequency-domain [20]:

$$\chi(\tau) = \mathcal{F}^{-1}\{\vartheta(\omega)\varsigma^*(\omega)\} \quad (2)$$

$$\vartheta(\omega) = \mathcal{F}\{\tilde{T}(t)\} \quad (3)$$

$$\varsigma(\omega) = \mathcal{F}\{\mathrm{W}(t)\tilde{S}(t)\} \quad (4)$$

where $\mathcal{F}$ and $\mathcal{F}^{-1}$ denote Fourier and inverse Fourier transform operators, respectively, (*) denotes the complex conjugate and W is a windowing function (e.g. Hanning window) used for reducing the side lobes when performing the cross-correlation in the frequency-domain. The output of operation $\chi(\tau)$ is a sinc-like function which compresses the energy of the whole signal under its main peak. The lag time of this main lobe is an emissivity-normalized quantity corresponding to the defect's depth, and it is defined as:

$$lag_\chi = \tau|_{\chi(\tau)=\mathrm{Max}(\chi(\tau))} \quad (5)$$

Subsequently, the phase of cross-correlation φ_χ can be found which is another emissivity-normalized quantity. The phase is calculated by repeating the operation with a new reference waveform in which all spectral components are -90 degrees phase shifted using the Hilbert transform:

$$\varsigma_H(\omega) = \mathcal{F}\left\{\mathrm{W}(t)\mathcal{H}(\tilde{S}(t))\right\} = -i\mathrm{sgn}(\omega)\varsigma(\omega) \quad (6)$$

$$\chi_H(\tau) = \mathcal{F}^{-1}\{\vartheta(\omega)\varsigma_H^*(\omega)\} \quad (7)$$

$$\varphi_\chi = \tan^{-1}\left(\frac{\chi(\tau)}{\chi_H(\tau)}\right)\Bigg|_{\tau=0} \quad (8)$$

where sgn denotes the sign function. Obviously, in the case of mono-frequency harmonic excitation, the calculated phase reduces to the phase of lock-in thermography (LT). The lag and phase calculated for the special case of LT are denoted as lag_{LT} and φ_{LT} respectively, in this manuscript.

For radio wave radar application, the pulse compression efficiency of the waveform is normally determined by calculating its auto-correlation (i.e. self cross-correlation) as follows:

DOI: https://doi.org/10.1016/j.ymssp.2019.07.011

$$\chi_{Auto}(\tau) = \tilde{S}(t) \otimes \tilde{S}(t+\tau) \quad (9)$$

In this research, the auto-correlation (Eq. 9) is calculated as a reference for the thermal cross-correlation of TWR (Eq. 1).

3. Frequency-phase modulated (FPM) waveform for maximized depth resolvability

3.1. Thermal frequency response (1D analysis)

The thermal frequency response θ for an anisotropic solid, in the absence of internal heating sources, can be defined by the following parabolic differential equation [24]:

$$\boldsymbol{\nabla} \cdot \left(\boldsymbol{\alpha} \cdot \boldsymbol{\nabla}\theta(\mathbf{r},\omega)\right) - i\omega\,\theta(\mathbf{r},\omega) = 0 \quad (10)$$

where $\omega = 2\pi f$ is the angular frequency [1/s], $\mathbf{r} = [x\ y\ z]$ is the spatial vector [m], $\boldsymbol{\nabla}$ is the nabla gradient operator, $i = \sqrt{-1}$ and $\boldsymbol{\alpha}$ is the tensor of anisotropic thermal diffusivity [m^2/s] :

$$\boldsymbol{\alpha} = \frac{\mathbf{k}}{\rho c_p} \quad (11)$$

Here $\mathbf{k}$ is the second order tensor of the anisotropic conductivity [W/m.K], ρ is the density [kg/m^3] and c_p is the heat capacity [J/kg.K] at constant pressure. By assuming 1D heat diffusion through the thickness (along z-axis) of a homogeneous solid, Eq. 10 reduces to:

$$\frac{\partial^2\theta(z,\omega)}{\partial z^2} - \beta^2\theta(z,\omega) = 0 \quad (12)$$

where the through-the-thickness diffusion length is $\mu_z(\omega) = \sqrt{2\alpha_z/\omega}$ and $\beta(\omega) = (1+i)/\mu_z(\omega)$. The inspection surface ($z = 0$) is subjected to an excitation $q(\omega)$ (i.e. $\frac{\partial\,\theta(z,\omega)}{\partial z}\Big|_{z=0} = -\frac{q(\omega)}{k_z}$) and there is no heat dissipation from the backside at a thickness h (i.e. $\frac{\partial\,\theta(z,\omega)}{\partial z}\Big|_{z=h} = 0$). Therefore, the solution of the governing homogenous second order partial differential equation can be derived as:

$$\theta(z,\omega) = A(\omega)\exp(\beta(\omega)z) + B(\omega)\exp(-\beta(\omega)z) \quad (13)$$

$$A(\omega) = \frac{q(\omega)}{\beta(\omega)k_z}\,\frac{\exp(-2\beta(\omega)h)}{1-\exp(-2\beta(\omega)h)} \quad (14)$$

$$B(\omega) = \frac{q(\omega)}{\beta(\omega)k_z}\,\frac{1}{1-\exp(-2\beta(\omega)h)} \quad (15)$$

For a given excitation waveform $\tilde{S}(t)$ and heating amplitude q_0, the relevant heating load in the frequency-domain is calculated as:

$$q(\omega) = \mathcal{F}\{q_0\tilde{S}(t)\} \quad (16)$$

and the corresponding time-domain thermal response at the inspection surface is derived by:

$$\tilde{T}(t) = \mathcal{F}^{-1}\{\theta(0,\omega)\} \quad (17)$$

The surface temperature $\tilde{T}$ may be calculated for the full thickness h as a non-defected area, or for any thinner thickness as the intermediate reflecting interface of a defected area.

DOI: https://doi.org/10.1016/j.ymssp.2019.07.011

3.2. The novel FPM waveform versus conventional waveforms

The proposed FPM waveform is formulated based on a central frequency f_c and a bandwidth $[f_1, f_2]$. The waveform is modulated by a 5 bit discrete coding which splits it into 5 sub-pulses at evenly spaced time spans so that the total burst time is $t_b = 5/f_c$ long, as follows:

$$[f_1, f_2] = [f_c(1+r), f_c(1-r)]\ ;\ r = 0.33 \tag{18}$$

$$\boldsymbol{C_f} = [1.00\ \ 0.75\ 0.5\ 0.25\ \ 0.00] \tag{19}$$

$$\boldsymbol{C_\varphi} = [C_{\varphi1}, C_{\varphi2}, C_{\varphi3}, C_{\varphi4}, C_{\varphi5}]\ ;\ \ -1 \le C_{\varphi j} \le 1 \tag{20}$$

$$P_j(\mathrm{t}) = \begin{cases} 1 & ; \\ 0 & ; \end{cases} \begin{matrix} (j-1)/f_c \le t < j/f_c \\ \text{else} \end{matrix} \tag{21}$$

$$\tilde{S}_{\mathrm{FPM}}(t) = \sum_{j=1}^{5} P_j(\mathrm{t}) \cos\left(2\pi\left(f_1 + (f_2 - f_1)C_{fj}\right)t + \frac{\pi}{2}C_{\varphi j}\right) \tag{22}$$

The frequency modulation code $\boldsymbol{C_f}$ (Eq. 19) has a constant definition such that it prescribes an evenly stepped modulation frequency from the upper band limit $f_c(1+0.33)$ to the lower band limit $f_c(1-0.33)$ over a length of 5 bits. A descending frequency modulation rate is preferably applied so that the specimen's depth is consistently resolved by the increasing diffusion length of the excited thermal waves.

The phase modulation code $\boldsymbol{C_\varphi}$ (Eq. 20) has a variable definition. Each member $C_{\varphi j}$ of the phase code can take any real number in the range $[-1, +1]$ so that the resultant phase as defined in Eq. 22, varies in the range $[-\pi/2, +\pi/2]$. This variable phase code provides flexibility to tailor the performance of the FPM waveform for increased depth resolvability of TWR.

Figure 1 presents an arbitrarily generated FPM waveform (the top row) against a Barker coded waveform (the middle row) and a frequency modulated sweep waveform (the bottom row) with corresponding thermal responses and calculated cross-correlations.

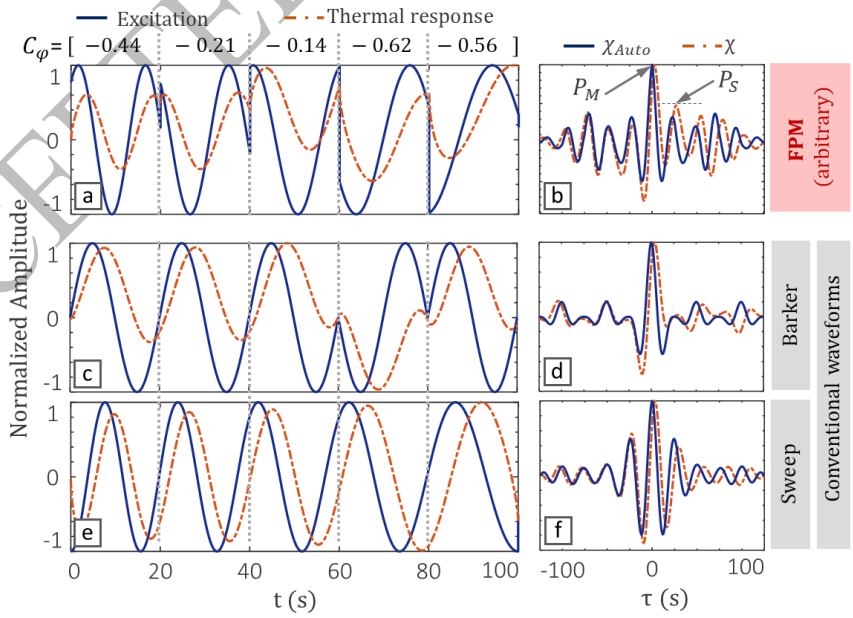

Figure 1: (a,c,e) Modulated excitation waveforms at a central frequency 0.05 Hz and resultant surface thermal response of a GFRP sample with a defect at a depth of 2 mm, and (b,d,f) corresponding auto-correlation (Eq. 9) and thermal cross-correlation (Eq. 1); P_M is the amplitude of the main peak of χ, and P_S is the amplitude of the largest side peak in the feasible range of the lag (i.e. $\tau > 0$)

DOI: https://doi.org/10.1016/j.ymssp.2019.07.011

The three waveforms presented in Figure 1 are generated at the same central frequency of 0.05 Hz and for the same 5 bit length of 100 s. The thermal responses correspond to a GFRP with a through-the-thickness diffusivity of $\alpha_z = 2.76 \times 10^{-7}$ m^2/s (see Table 1 in section 4) having a defect (i.e. reflector) at a depth of 2 mm (i.e. 8 plies deep).

The arbitrary FPM waveform corresponds to a randomly generated phase code (see Figure 1(a)), and the 5 bit Barker coded waveform (Figure 1(c)) is in fact a mono-frequency harmonic signal in which the 4th bit is 180 degrees phase shifted (i.e. a particular FPM with $r = 0$ and $\boldsymbol{C_\varphi} = [-1,-1,-1,+1,-1]$). The sweep waveform (Figure 1(e)) is generated by a linear frequency modulation with the same frequency bandwidth $[f_1, f_2]$ and burst time t_b of the FPM as follows:

$$f(t) = f_1 + \left(\frac{f_2 - f_1}{2t_b}\right) t \tag{23}$$

$$\tilde{S}_{\text{Sweep}}(t) = cos(2\pi f(t).t - \pi) \tag{24}$$

The calculated thermal cross-correlations as shown in Figure 1(b,d,f) indicate the distortion, the asymmetry and the peak delay (compared with the auto-correlation) induced by the thermal response. Moreover, the results demonstrate the relatively low sidelobe (i.e. noise) level of Barker coded waveform compared to the other two waveforms indicating its good pulse compression quality. Indeed, a lower peak-sidelobe-level implies a lower noise level and consequently a higher SNR in the output of the matched filter.

Furthermore, the depth resolvability of the modulated waveforms with respect to LT is demonstrated in Figure 2 in terms of (a) lag and (b) phase contrast (compared to a non-defected 4 mm thick GFRP). The left axes correspond to the absolute contrast quantity (bulleted line) obtained from LT (i.e. a mono-frequency harmonic excitation) as a reference, and the right axes correspond to the deviation of the absolute contrast quantity of modulated waveforms from this reference. Therefore, a positive value at the right axis indicates outperformance compared to LT, and vice versa. The results indicate that lag and phase of LT resolve the depth down to around 2 mm (half thickness). The Barker coded waveform has the highest performance among modulated waveforms. The sweep waveform barely improves the depth resolvability, while the arbitrarily modulated FPM waveform leads to a significant enhancement of depth resolvability.

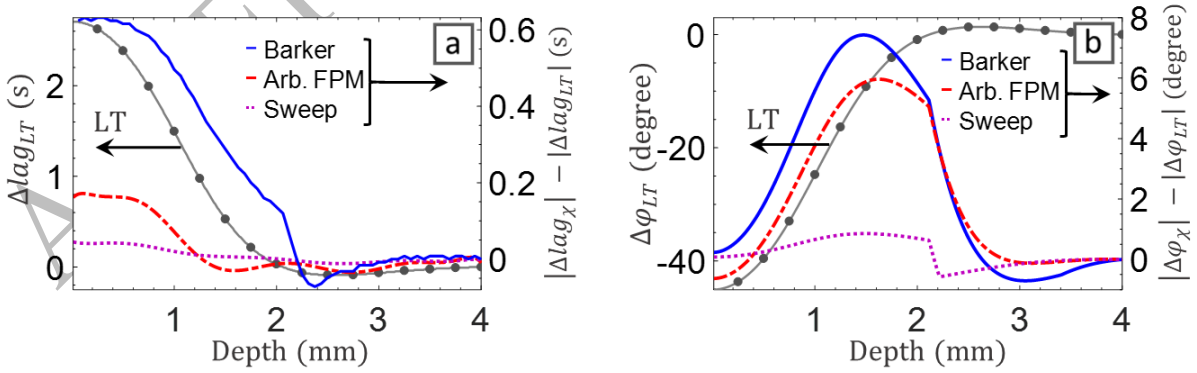

Figure 2: Depth resolvability of the evaluated modulated waveforms (presented in Figure 1) compared to LT (central frequency 0.05 Hz) in terms of (a) lag contrast and (b) phase contrast

DOI: https://doi.org/10.1016/j.ymssp.2019.07.011

3.3. Exploring the search space for the supreme FPM waveforms

In section 3.2, a FPM waveform was introduced with a constant frequency code definition but a variable phase code with float real valued elements. An arbitrarily generated phase code showed the potential of improving depth resolvability of the FPM waveform compared to LT (Figure 2). The aim of this section is to explore a randomly generated search space for an optimized phase code such that its performance is maximized in terms of pulse compression and defect-induced contrast of phase or lag.

The quality of pulse compression is normally determined by the peak-sidelobe-level (PSL) of the cross-correlation. Minimization of PSL ensures high SNR in the output of the matched filter and therefore reduces ambiguity in the calculation of the lag with the presence of stochastic noise. Hence, the pulse compression quality of TWR is determined by the PSL of the thermal cross-correlation (of a defect with an intermediate depth $z = 0.5h$) which needs to be minimized:

$$\mathrm{PSL} = 20\log_{10}\left(\frac{P_S}{P_M}\right)\Big|_{z=0.5h} \tag{25}$$

Here $P_M = \max(\chi(\tau))$ is the amplitude of the main peak of χ, and P_S is the amplitude of the largest side peak (see Figure 1(b)) in the feasible range of the lag (i.e. $\tau > 0$ for a time causal system). The PSL of the auto-correlation χ_{Auto} is also calculated herein as a reference and denoted by $\mathrm{PSL}_{\mathrm{Auto}}$.

Moreover, the depth resolvability of lag and phase are, respectively, determined by the following objective functions to be maximized:

$$F_{lag} = \frac{1}{h}\int_0^h \left(\left|\Delta lag_{\chi}(z)\right| - \left|\Delta lag_{LT}(z)\right|\right) dz \tag{26}$$

$$F_{\varphi} = \frac{1}{h}\int_0^h \left(\left|\Delta \varphi_{\chi}(z)\right| - \left|\Delta \varphi_{LT}(z)\right|\right) dz \tag{27}$$

These objective functions determine the deviation of the absolute contrast quantity (lag or phase) from that of LT (see right axes of Figure 2), averaged through the depth. This provides a measure of the FPM waveform's performance compared to LT.

A relatively large population of 20,000 FPM waveforms with randomly generated phase codes are examined through the 1D analytical solution. A central frequency of 0.05 Hz is applied and the search space is evaluated through the quantities defined in Eq. 25-27 (see Figure 3). The relative location of the conventional modulated waveforms (Barker and sweep), the arbitrary FPM waveform (see Figure 1) and also LT are indicated in the search space for comparison. As expected, among these reference waveforms, the Barker coded one shows the highest performance [15, 23]. However, this Barker coded waveform is dominated by a multitude of the FPM waveforms introduced in the search space.

The distribution of F_{lag} versus PSL for the whole population is shown in Figure 3(a) in which the individual denoted as FPM1 corresponds to the highest F_{lag} achieved at the lowest PSL. Therefore, FPM1 is picked as a supreme waveform. Likewise, Figure 3(b) presents the distribution of F_{φ} versus PSL for the whole population in which FPM1 is approaching the upper extreme of F_{φ} confirming its superior depth resolvability in terms of both lag and phase. The pulse compression quality (as measured by PSL) only contributes to a reduced ambiguity in the calculation of the lag.

DOI: https://doi.org/10.1016/j.ymssp.2019.07.011

Therefore, the individual with the highest F_φ, denoted as FPM2, is also picked as another supreme waveform with maximum depth resolvability of phase, despite its relatively low pulse compression quality (i.e. high PSL).

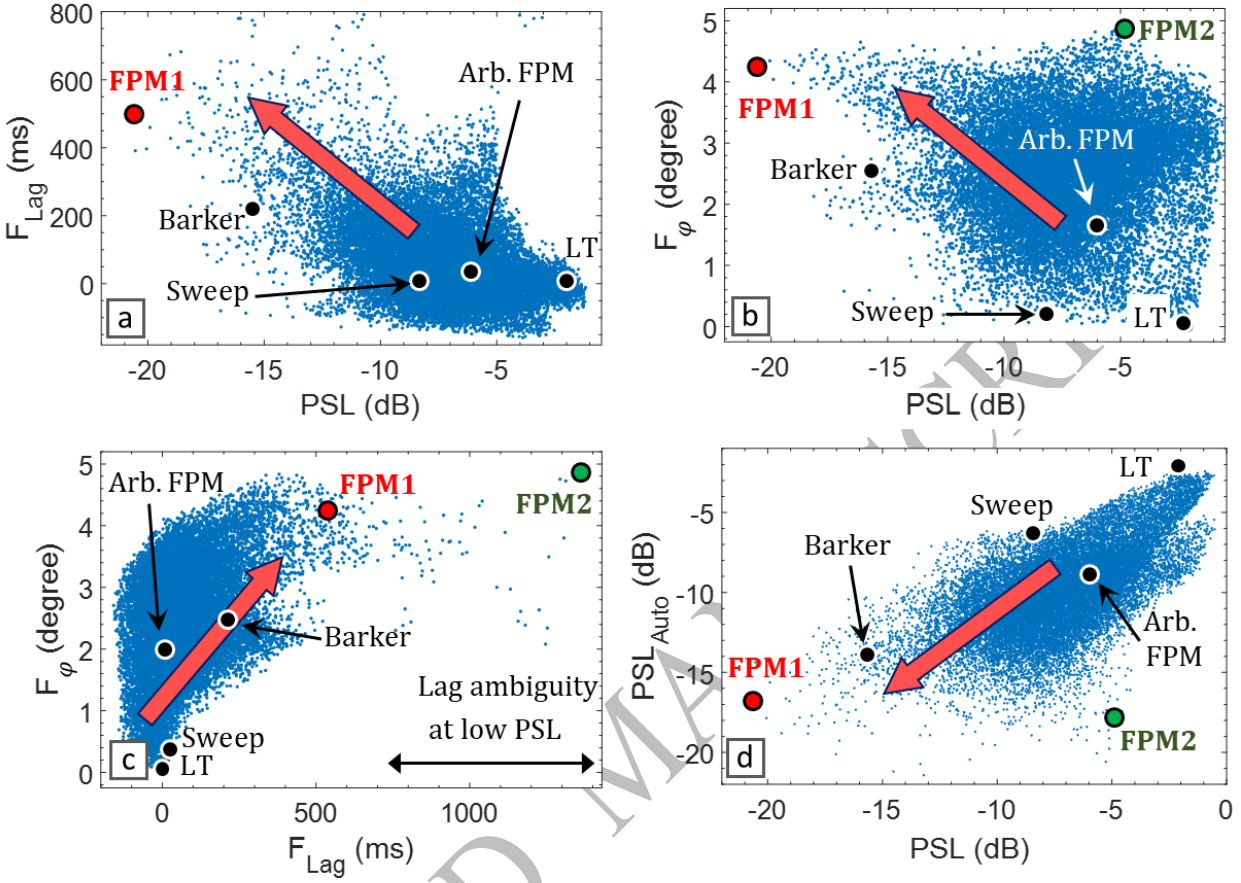

Figure 3: Search space corresponding to a population of 20,000 randomly generated FPM waveforms, and relative location of the selected supreme waveforms FPM1 and FPM2 compared to sweep, Barker coded and an arbitrary FPM waveform (see Figure 1(a,c,e)).

Figure 3(c) presents the distribution of F_φ versus F_{lag} in which the lag ambiguity of individuals with relatively high PSL (e.g. FPM2) is evidenced by the scattered overestimations of F_{lag} at its upper extreme. The relative values of PSL and PSL_{Auto} are also demonstrated in Figure 3(d) which clearly confirm that a low PSL_{Auto} does not necessarily ensure a low PSL of TWR. Although FPM2 has a lower PSL_{Auto} than FPM1, its PSL is much higher and leads to ambiguity in the determination of lag as presented in Figure 3(c).

3.4. Evaluation of the selected supreme waveforms FPM1 and FPM2

The selected waveforms FPM1 and FPM2, and their corresponding phase codes and calculated cross-correlations are presented in Figure 4. As expected from Figure 3(d), FPM2 has a high sidelobe level leading to its increased PSL compared to FPM1.

Furthermore, the resultant depth resolvability of the two supreme waveforms FPM1 and FPM2 are evaluated and compared with the Barker coded waveform (which showed the highest performance in Figure 2) as shown in Figure 5 in terms of (a) lag contrast and (b) phase contrast. Comparing the results presented in Figure 2 and Figure 5 clearly confirms that proper phase modulation of the FPM waveform leads to a significantly higher depth resolvability than that of

DOI: https://doi.org/10.1016/j.ymssp.2019.07.011

conventional modulated waveforms. Among the two supreme waveforms, FPM1 results in a higher depth resolvability of the lag (Figure 5(a)) and FPM2 results in a higher depth resolvability of the phase (Figure 5(b)). In terms of depth resolvability through lag, FPM1 and FMP2 both outperform the Barker coded waveform, down to around 2 mm deep after which they converge and decline to slightly below zero (i.e. result in a lag contrast smaller than LT).

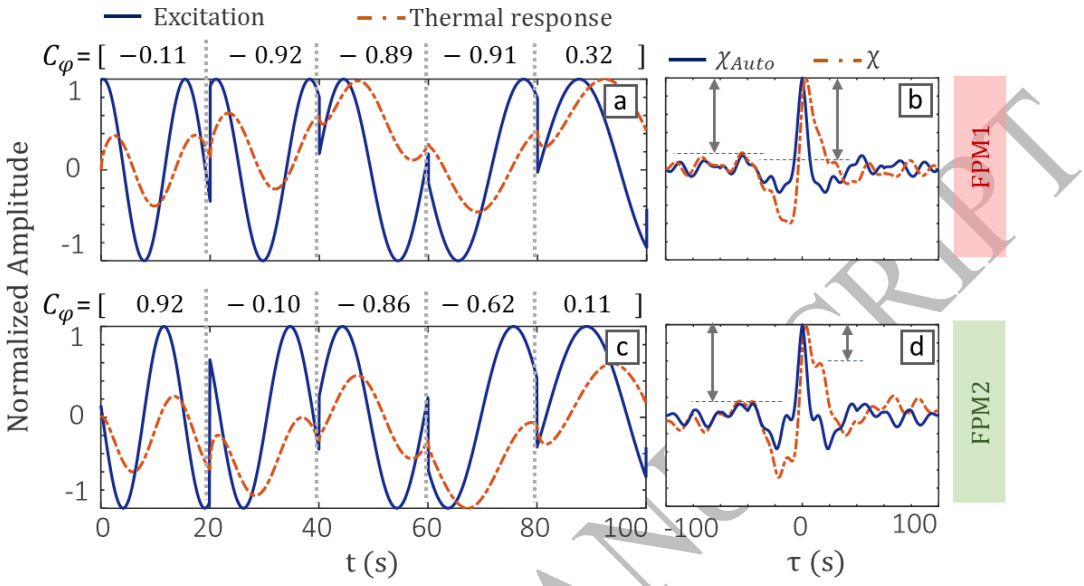

Figure 4: Selected supreme waveforms (a) FPM1 and (c) FPM2 at a central frequency 0.05 Hz and resultant thermal response at the surface of a GFRP sample with a defect at a depth of 2 mm, and (b,d) corresponding auto-correlation (Eq. 9) and thermal cross-correlation (Eq. 1)

However, in terms of depth resolvability through phase, both FPM1 and FMP2 outperform the Barker coded waveform and are able to resolve the entire depth (down to 4 mm deep) while the Barker coded waveform drops to below zero (i.e. results in a phase contrast less than LT) at 2.6 mm depth.

As presented in Figure 5(a) the high PSL of FPM2 leads to ambiguity in the detection of the lag corresponding to shallow defects ($z < 0.6$ mm). This explains why F_{lag} of FPM2 is highly overestimated in the search space shown in Figure 3(c).

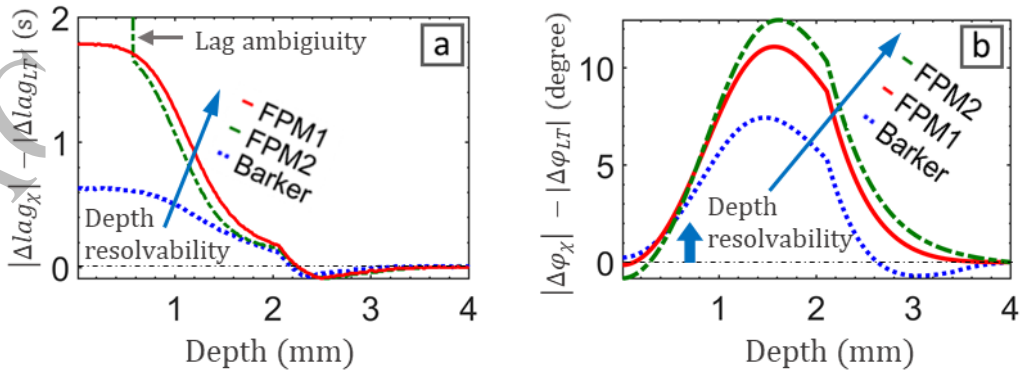

Figure 5: Depth resolvability of the selected waveforms FPM1 and FPM2 (presented in Figure 4) and the Barker code compared to LT in terms of (a) lag contrast and (b) phase contrast

DOI: https://doi.org/10.1016/j.ymssp.2019.07.011

4. Application to the 3D thermal wave problem (FE simulation)

The 1D analytical solution used in section 3 enabled fast calculation of the thermal response, providing an efficient evaluation of the random search space. However, the 1D approach is valid for thermal diffusion towards the defect (on the condition that the inspection surface is uniformly heated), but not for the 3D heat diffusion of the heat wave reflected back from the defect. In this section, the performance of FPM1 and FPM2 in the inspection of a GFRP laminate is evaluated based on a 3D FE simulation. Realistic conditions are taken into account: heat dissipation to the surrounding environment, non-uniform heating induced by the optical source and more importantly the measurement noise of the infrared camera.

A 4 mm thick GFRP laminate with quasi-isotropic lay-up $[(+45/0/-45/90)]_{2s}$ as schematically shown in Figure 6 is modelled by Abaqus/CAE using brick elements with quadratic shape functions (a total number of 134,487 elements). The laminate includes six interply defects (i.e. delaminations) defined as 10 mm wide square interfaces with nodal disbond (i.e. no thermal interaction). Two 2 kW optical sources with 45° beam angle are assumed at a standoff distance of 500 mm from the sample and (to induce an asymmetric heating pattern) at an offset of 300 mm from its centerline. The radiative heat flux emitted to the sample's surface is calculated by assuming a Gaussian distribution of the heating intensity and a uniform emissivity coefficient of 0.9. For more details concerning the FE model the reader is referred to [25].

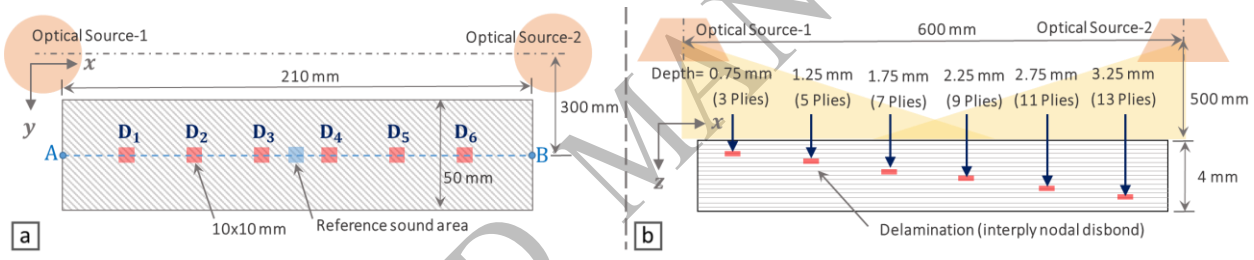

Figure 6: Schematic presentation of simulated quasi-isotropic GFRP laminate $[(+45/0/-45/90)]_{2s}$ and assumed position of optical sources (a) top view and (b) side view

The assumed material properties of glass fiber and epoxy resin and resultant diffusivities calculated for a GFRP with 50% volume fraction of glass are given in Table 1. The effective thermal diffusivity calculated along fibers is 1.63 times higher than normal to the fibers which thus leads to a dominant lateral (in-plane) heat diffusion.

Table 1: Thermo-physical properties calculated [26] for a unidirectional GFRP ply with 50% volume fraction of glass fibers (x' and y' denote the local ply axes along and perpendicular to the fibers, respectively)

Material	ρ (kg/m^3)	C_p (J/kg K)	$k_{x'}$ (W/m K)	$k_{y'}, k_z$ (W/m K)	$\alpha_{x'}$ (m^2/s)	$\alpha_{y'}, \alpha_z$ (m^2/s)
Glass fiber	2460	740	1.25	1.25	6.87×10^{-7}	6.87×10^{-7}
Epoxy resin	1160	1100	0.24	0.24	1.88×10^{-7}	1.88×10^{-7}
GFRP	1810	920	0.75	0.46	4.50×10^{-7}	2.76×10^{-7}

The calculated thermal response is degraded with a temporal Gaussian white noise of standard deviation 20 mK, which is equal to the noise equivalent differential temperature (NEDT) of a high-end infrared camera. A 10 mm wide square area at the center of the sample (see Figure 6(a)) is

DOI: https://doi.org/10.1016/j.ymssp.2019.07.011

selected and its mean value is used as a reference to calculate the corresponding contrast quantities (phase or lag) as presented in Figure 7.

The contour map of the lag and phase contrast for FPM1 are shown in Figure 7(a) and (b), respectively. Note that the effect of non-uniform heating is cancelled out in these representations. Furthermore, the gradient of the lag and phase contrast along the centerline of the defects (line AB) and in the vicinity of the defects are shown in Figure 7(c) and (d), respectively. The contrast obtained through FPM1, FPM2 and the Barker coded excitation waveforms are compared with that of LT at the central frequency 0.05 Hz. A good agreement with the results of Figure 5 is observed, indicating that the observations made in the 1D model are equally valid for the 3D model. The very poor contrast obtained through LT at the intermediate defect D4, confirms that it is being inspected at a frequency close to the so-called blind frequency (i.e. the frequency associated with a zero-crossing of the defect-induced phase contrast). However, due to the in-plane phase gradient induced by the lateral heat diffusion, a zero phase contrast may not be achievable over the entire defected area unless buried under the noise level.

According to Figure 7(c), the lag contrast of the waveforms FPM1 and FPM2 is consistently higher than that of the Barker coded waveform, and all modulated waveforms consistently outperform LT down to D4 (2.25 mm deep). Inspecting D4 at a central frequency close to its blind frequency shows the true capability of TWR. Each modulated waveform shows good contrast, with the FPM1 having a contrast almost double of the contrast in the Barker coded waveform, while LT leads to very poor lag contrast. The deeper defects D5 and D6 which are inspected at a frequency higher than their blind frequency, lead to a negative lag contrast through LT, a comparable contrast through the FPM waveforms, and a very poor contrast through the Barker coded waveform.

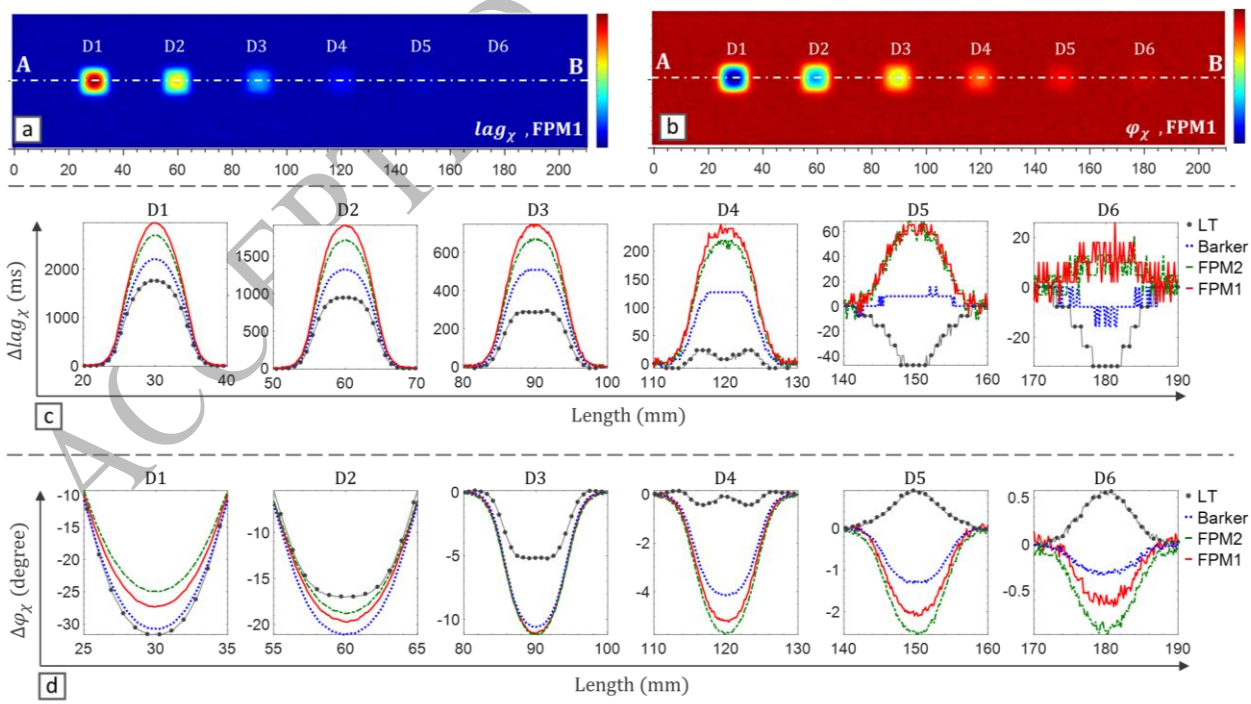

Figure 7: FEA results corresponding to the inspection of the GFRP laminate shown in Figure 6 at the central frequency 0.05 Hz and for an NEDT of 20 mK: (a) lag image and (b) phase image obtained from the selected waveform FPM1, and comparison of the depth resolvability of the various waveforms along the centerline of the defects (line AB) in terms of (c) lag contrast and (d) phase contrast

DOI: https://doi.org/10.1016/j.ymssp.2019.07.011

According to Figure 7(d), and as expected from Figure 5(b), the phase contrast obtained from the FPM waveforms is initially lower for the relatively shallow defects D1 and D2 when compared to the phase contrast from the LT and the Barker coded waveforms. However, for deeper defects, the FPM waveform leads to a higher phase contrast. Moreover, FPM2 which results in a slightly lower lag contrast than FPM1 (Figure 7(c)), outperforms FMP1 in terms of phase contrast, confirming the results shown in Figure 5.

Despite the very low pulse compression quality (i.e. high PSL) of FPM2, the results suggest that it can capably resolve the depth by reliable determination of the lag in the presence of stochastic noise. However, the ambiguity induced by the noise level also depends on the dominance of the lag contrast (i.e. the thermal diffusivity mismatch introduced by the defect's interfaces). In fact, any heat leakage through the defect (e.g. due to a partial contact or presence of a filling material) reduces the resultant lag contrast and makes it more dominated by the noise (compared to the ideal disbond condition considered in the FE simulation).

In order to further study this matter, the contrast quantities of each defect (averaged over the defect area) obtained through the different waveforms are determined at a relatively high noise level (i.e. NEDT of 200 mK) as presented in Figure 8. Moreover, the variations of contrast quantities with respect to the noise level (i.e. NEDT of 0-200 mK) are presented in the insets of Figure 8, for the intermediate defect D4. Each noise level is applied in 10 iterations and the corresponding deviation range around the average value is indicated by the error bars.

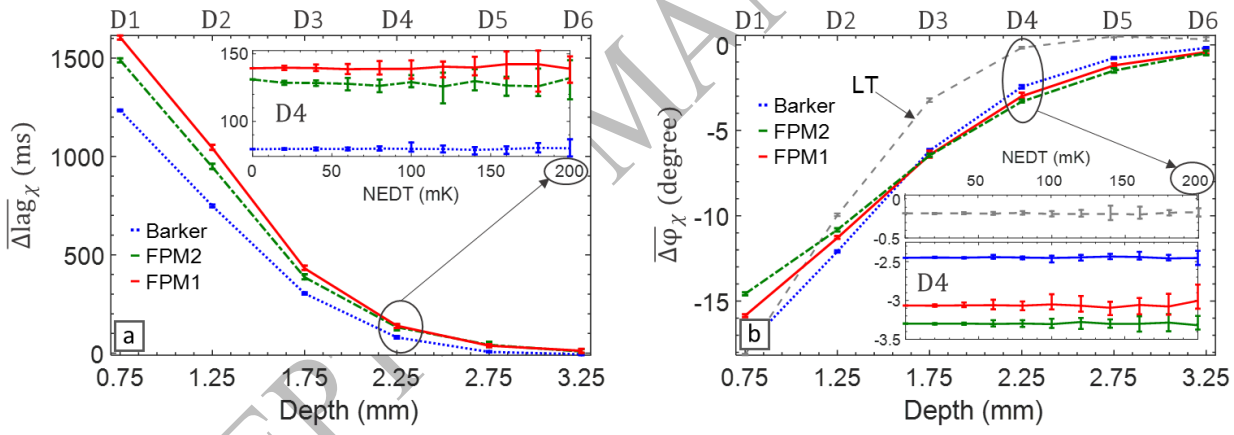

Figure 8: The average contrast quantity (a) lag and (b) phase subject to a high noise level (NEDT of 200 mK); the insets present the gradient of the contrast quantity for defect D4 versus NEDT and the error bars indicate the deviation range corresponding to 10 iterations of applying random noise

According to Figure 8(a), FPM2 shows a good stability comparable to FPM1 in determination of the lag for an NEDT of up to 200 mK. The Barker coded waveform has a lower deviation range than the FPM waveforms, due to its periodic definition which has a noise averaging characteristic. It is noteworthy that LT (which has the lowest pulse compression efficiency) leads to a very unstable calculation of lag at this high noise level with very wide deviations outside the range shown in Figure 8(a). Therefore, it has been excluded from this figure.

Likewise, Figure 8(b) confirms the good performance and stability of the FPM waveforms in calculation of the phase contrast, and again a lower deviation range is observed for the Barker coded waveform and LT due to their periodic (noise averaging) nature. The very low sensitivity of the phase of LT to the noise level (Figure 8(b)) despite its very high PSL, clearly demonstrates the fact that the pulse compression quality has no contribution in the determination of phase.

DOI: https://doi.org/10.1016/j.ymssp.2019.07.011

5. Conclusions

A novel frequency-phase modulated (FPM) waveform was introduced and a framework was developed to adapt its variable modulation code for maximized depth resolvability of thermal wave radar (TWR). Initially, the thermal frequency response was calculated through a simplified 1D analytical solution for fast and efficient exploration of the search space in order to identify supreme FPM waveforms. Then the enhanced depth resolvability of the selected FPM waveforms, compared to conventional waveforms, was validated through 3D finite element simulation. Glass fiber reinforced polymer (GFRP) was assumed as an orthotropic constitutive material with dominant in-plane heat diffusion, to be inspected for detection of delaminations.

Two FPM waveforms were selected from the search space based on their maximized depth resolvability through resultant lag and phase in the output channel of TWR. Although FPM waveforms were explored based on a 1D analytical estimation of the thermal problem, their superior performance was maintained when inspecting a GFRP with dominant in-plane heat diffusion, and their robustness at various noise levels was demonstrated.

The fact that the introduced FPM waveforms can be easily coupled to an optimization procedure for improved efficiency and defect detectability, provides a unique opportunity to go beyond current limitations of optical infrared thermography for NDT of deep defects.

Acknowledgement

The authors acknowledge the SBO project DETECT-IV (Grant no. 160455), which fits in the SIM research program MacroModelMat (M3) coordinated by Siemens (Siemens PLM software, Belgium) and funded by SIM (Strategic Initiative Materials in Flanders) and VLAIO (Flemish government agency Flanders Innovation & Entrepreneurship). The authors also acknowledge Fonds voor Wetenschappelijk Onderzoek Vlaanderen (FWO-Vlaanderen) through grants 1148018N and 12T5418N.

References

1. Yang, R. and Y. He, *Optically and non-optically excited thermography for composites: A review.* Infrared Physics & Technology, 2016. **75**: p. 26-50.
2. Ciampa, F., et al., *Recent advances in active infrared thermography for non-destructive testing of aerospace components.* Sensors, 2018. **18**(2): p. 609.
3. Zhao, Y., et al., *A novel defect depth measurement method based on Nonlinear System Identification for pulsed thermographic inspection.* Mechanical Systems and Signal Processing, 2017. **85**: p. 382-395.
4. Zhang, H., et al., *Enhanced Infrared Image Processing for Impacted Carbon/Glass Fiber-Reinforced Composite Evaluation.* Sensors, 2017. **18**(1): p. 45.
5. Tavakolian, P., K. Sivagurunathan, and A. Mandelis, *Enhanced truncated-correlation photothermal coherence tomography with application to deep subsurface defect imaging and 3-dimensional reconstructions.* Journal of Applied Physics, 2017. **122**(2): p. 023103.
6. Xu, C., et al., *Improving defect visibility in square pulse thermography of metallic components using correlation analysis.* Mechanical Systems and Signal Processing, 2018. **103**: p. 162-173.
7. Mulaveesala, R., J.S. Vaddi, and P. Singh, *Pulse compression approach to infrared nondestructive characterization.* Review of Scientific Instruments, 2008. **79**(9): p. 094901.
8. Tabatabaei, N. and A. Mandelis, *Thermal-wave radar: A novel subsurface imaging modality with extended depth-resolution dynamic range.* Review of Scientific Instruments, 2009. **80**(3): p. 034902.

9. Tabatabaei, N. and A. Mandelis, *Thermal coherence tomography using match filter binary phase coded diffusion waves.* Physical review letters, 2011. **107**(16): p. 165901.
10. Tabatabaei, N., A. Mandelis, and B.T. Amaechi, *Thermophotonic radar imaging: An emissivity-normalized modality with advantages over phase lock-in thermography.* Applied Physics Letters, 2011. **98**(16): p. 163706.
11. Gong, J., et al., *Investigation of carbon fiber reinforced polymer (CFRP) sheet with subsurface defects inspection using thermal-wave radar imaging (TWRI) based on the multi-transform technique.* NDT & E International, 2014. **62**: p. 130-136.
12. Silipigni, G., et al., *Optimization of the pulse-compression technique applied to the infrared thermography nondestructive evaluation.* NDT & E International, 2017. **87**: p. 100-110.
13. Shi, Q., et al., *Study on the Detection of CFRP Material with Subsurface Defects Using Barker-Coded Thermal Wave Imaging (BC-TWI) as a Nondestructive Inspection (NDI) Tool.* International Journal of Thermophysics, 2018. **39**(8): p. 92.
14. Laureti, S., et al., *Comparative study between linear and non-linear frequency-modulated pulse-compression thermography.* Applied Optics, 2018. **57**(18): p. D32-D39.
15. Shi, Q., et al., *Barker-coded Modulation Laser Thermography for CFRP Laminates Delamination Detection.* Infrared Physics & Technology, 2019.
16. Hedayatrasa, S., et al., *Performance of frequency and/or phase modulated excitation waveforms for optical infrared thermography of CFRPs through thermal wave radar: A simulation study.* Composite Structures, 2019: p. 111177.
17. Yang, R., et al., *Induction Infrared Thermography and Thermal-Wave-Radar Analysis for Imaging Inspection and Diagnosis of Blade Composites.* IEEE Transactions on Industrial Informatics, 2018. **14**(12): p. 5637-5647.
18. Yi, Q., et al., *New features for delamination depth evaluation in carbon fiber reinforced plastic materials using eddy current pulse-compression thermography.* NDT & E International, 2019. **102**: p. 264-273.
19. Nathanson, F.E., J.P. Reilly, and M.N. Cohen, *Radar design principles-Signal processing and the Environment.* NASA STI/Recon Technical Report A, 1991. **91**.
20. Mahafza, B.R., *Radar Systems Analysis and Design Using MATLAB Third Edition*. 2016: Chapman and Hall/CRC.
21. Bhamre, P. and S. Gupta. *A Review on Poly-Phase Coded Waveforms for MIMO Radar with Increased Orthogonality*. in *International Conference on Future Internet Technologies and Trends*. 2017. Springer.
22. Mohr, C.A., et al. *Spectrally-efficient FM noise radar waveforms optimized in the logarithmic domain*. in *Radar Conference (RadarConf18), 2018 IEEE*. 2018. IEEE.
23. Tabatabaei, N., *Matched-Filter Thermography.* Applied Sciences, 2018. **8**(4): p. 581.
24. Hahn, D.W. and M.N. Özisik, *Heat conduction*. 2012: John Wiley & Sons.
25. Hedayatrasa, S., et al., *On Efficient FE Simulation of Pulse Infrared Thermography for Inspection of CFRPs*, in *14th Quantitative InfraRed Thermography Conference*. 2018.
26. Springer, G.S. and S.W. Tsai, *Thermal conductivities of unidirectional materials.* Journal of Composite Materials, 1967. **1**(2): p. 166-173.